PAPER

Design principles for wave plate metasurfaces using plasmonic L-shaped nanoantennas

To cite this article: Asad A Tahir *et al* 2017 *J. Opt.* **19** 035001

View the article online for updates and enhancements.

Design principles for wave plate metasurfaces using plasmonic L-shaped nanoantennas

Asad A Tahir[1]**, Sebastian A Schulz**[1]**, Israel De Leon**[1,2] **and Robert W Boyd**[1,3]

[1] Department of Physics, University of Ottawa, 25 Templeton Street, Ottawa, K1N 6N5, Ontario, Canada
[2] School of Engineering and Science, Tecnológico de Monterrey, Monterrey, Nuevo León 64849, Mexico
[3] Institute of Optics and Department of Physics and Astronomy, University of Rochester, 275 Hutchison Rd., Rochester, NY 14627, United States of America

E-mail: ideleon@itesm.mx

Abstract

Plasmonic L-shaped antennas are an important building block of metasurfaces and have been used to fabricate ultra-thin wave plates. In this work we present principles that can be used to design wave plates at a wavelength of choice and for diverse application requirements using arrays of L-shaped plasmonic antennas. We derive these design principles by studying the behavior of the vast parameter space of these antenna arrays. We show that there are two distinct regimes: a weak inter-particle coupling and a strong inter-particle coupling regime. We describe the behavior of the antenna array in each regime with regards to wave plate functionality, without resorting to approximate theoretical models. Our work is the first to explain these design principles and serves as a guide for designing wave plates for specific application requirements using plasmonic L-shaped antenna arrays.

Keywords: optical design, metamaterials, plasmonics, birefringence, wave plate, nanophotonics

(Some figures may appear in colour only in the online journal)

1. Introduction

Wave plates are ubiquitous elements in optics, with conventional applications to polarization rotation and with more recent applications to Pancharatnam–Berry phase optical elements (PBOEs) such as the q-plate [1]. With the advent of nanophotonics, there has been an increasing interest in manipulating the phase and polarization of light at the nanoscale using surface plasmons [2–12]. As such, substantial work has been done in realizing plasmonic wave plates, often based on structures which support two orthogonal plasmonic eigenmodes [13–21]. The symmetry axes of these eigenmodes play the role of the principal axes of birefringent media used to make conventional wave plates. They are thus tailored to scatter light with equal amplitude and an appropriate phase difference, such as π for a half-wave plate, at the desired excitation wavelength. However, due to the finite linewidth of these eigenmodes, plasmonic wave plates often have a limited

bandwidth. They traditionally also have low efficiencies due in part to inherent dissipative effects in plasmonic structures. For instance, the best reported half-wave plate efficiency, for single-layered planar plasmonic structures less than 100 nm thick, is 20% [16]. More recently though, multi-layered plasmonic structures have been demonstrated that work as broadband, high-efficiency wave plates and are well suited for applications that work in reflection [22–25]. However, working in reflection is not suitable for some applications. In addition to the above, there have been recent developments to realize optically active plasmonic metasurfaces [26–28].

A structure of considerable interest for ultrathin, single-layered plasmonic metasurfaces is the L-shaped nanoantenna [29–37]. It supports two orthogonal eigenmodes, which are identified in figure 1 as the symmetric mode and the anti-symmetric mode. The symmetric mode is excited by light polarized along the symmetric axis and supports dipolar currents along each arm of the antenna. The antisymmetric
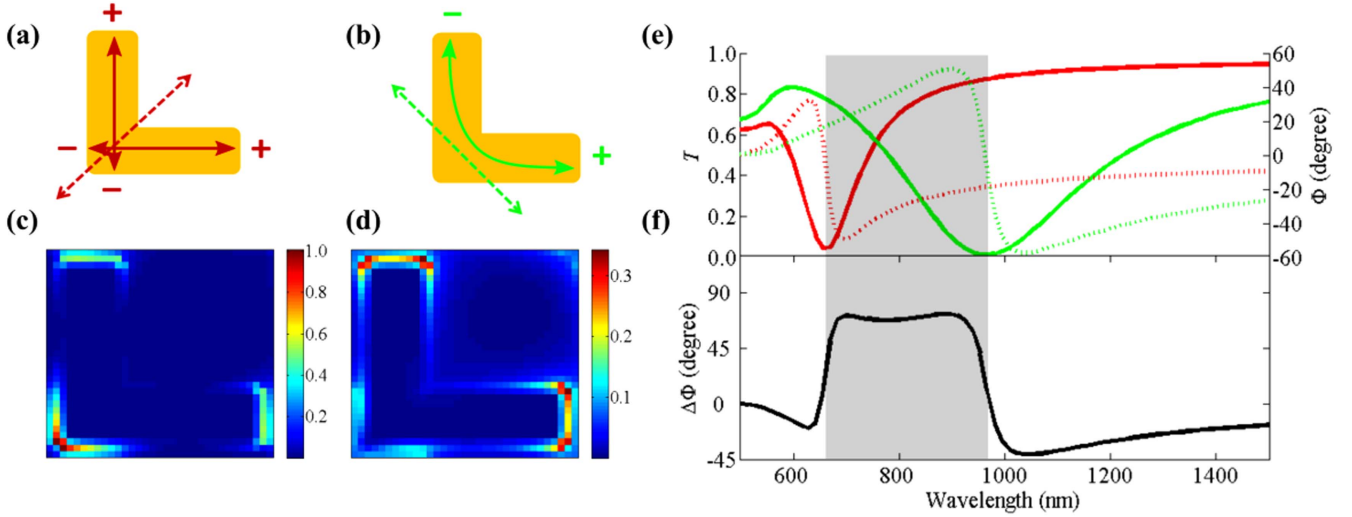
Figure 1. The excitation axis (dotted arrow) and dipolar currents (solid arrows) for (a) the symmetric eigenmode and (b) the antisymmetric eigenmode. The field distribution on an individual antenna for (c) the symmetric eigenmode and (d) the antisymmetric eigenmode. (e) Transmission spectrum, T (solid line) and phase, Φ (dotted) of the symmetric (red) and antisymmetric (green) eigenmode. (f) The phase difference, $\Delta\Phi$, between light scattered from each eigenmode. The shaded region in (e) and (f) indicates the spectral region between the two resonances, in which a phase difference can be incurred.

mode is excited by light polarized along the antisymmetric axis and supports dipolar currents which span across both arms of the antenna. The eigenmodes introduce a phase shift between the incident and scattered fields. The phase difference, $\Delta\Phi$, between the fields scattered from the eigenmodes, peaks between their resonance centers, hitherto referred to as the overlap region and shaded gray in figure 1(e). Hence the spectral gap between the resonances affects the width and magnitude of the $\Delta\Phi$ profile.

The anisotropy of these antennas was first demonstrated by Xu *et al* [29] and has been used to realize wave plates [30–32], phased arrays [33] and plasmonic q-plates [34, 35]. Theoretical models for the amplitude and phase response of these antennas have been proposed. However, these consider a thin-wire approximation [36], which is not always accurate for 'fat' antennas having a small ratio of arm length to width. Moreover, they do not consider strong inter-particle coupling between antennas in an array [36, 37], which is an important regime to consider for metasurface-based wave plates [26]. Also, previous works on L-shaped antennas do not consider the effect of varying array parameters, such as the lattice constant and the array topology, on wave plate functionality.

In order to study the response of these antenna arrays while fully utilizing their vast parameter space, a full vectorial wave solution, such as the finite difference time domain method (FDTD), is required. This is particularly important when studying arrays with strong inter-antenna coupling and antennas with small arm length to width ratio, for which simplified theoretical models are inadequate. However, due to the fine mesh resolution required to accurately model plasmonic structures using numerical methods, designing ultra-thin plasmonic wave plates using the vast parameter space of L-shaped nanoantennas can be time consuming. It is therefore very important to have design principles that guide the design of wave plates with desired performance characteristics. In

this work, we report design principles for periodic arrays of L-shaped nanoantennas to realize plasmonic half-wave plates in transmission. We derive these principles after explaining the behavior of the parameter space of these antenna arrays, which helps the reader develop insights into the properties of these antenna arrays. The principles we present can be used to quickly design for a desired wavelength region, for specific application requirements or available fabrication processes. The parameter space we explore in this work includes the length, L, and width, w, of each arm of the antenna. Since practical plasmonic wave plates require arrays of nanostructures, we also explore the array parameters, specifically the lattice constant, a, and the array topology quantified by the angle θ (see figure 2).

While half-wave plate metasurfaces based on the L-antenna arrays we consider are less efficient as compared to quarter-wave plates, we performed this study for the former because of their application to q-plates and other PBOEs, which are of particular interest to the optics community [34, 35, 38–41]. However, the principles we present here are easily applicable to quarter-wave plate metasurfaces.

We use a commercial FDTD solver (Lumerical FDTD) [42] for our investigation. The structure we consider is a two dimensional, periodic array of 40 nm thick gold antennas on a semi-infinite glass substrate, where the dielectric constants of the gold and glass are taken from [43] and [44] respectively. The angle between the antenna arms is fixed at 90°. A mesh step of $\Delta x = 5$ nm, $\Delta y = 5$ nm and $\Delta z = 3$ nm is used for the span of the antenna. These settings provide mesh convergence (1% for transmission and 6% for the resonance wavelength).

Since half-wave plates invert the handedness of incident circularly polarized light, we assess the performance of our designs in transmission by defining as follows the purity, ρ, and the efficiency, η, for a right circularly polarized plane
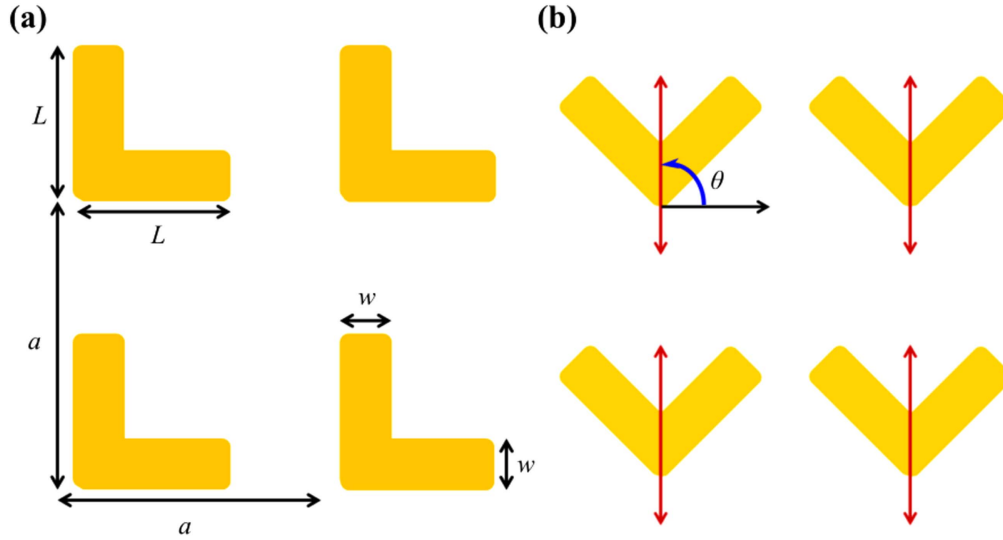
Figure 2. Parameters considered for our study. (a) The arm length *L*, the arm width *w* and the lattice constant *a*. (b) Topology quantified by angle θ from horizontal to symmetric axis (red arrow).

wave input at normal incidence:

$$\rho = \frac{P_{\text{LC}}}{P_{\text{T}}}, \tag{1}$$

$$\eta = \frac{P_{\text{LC}}}{P_{\text{I}}} = \rho T, \tag{2}$$

where P_{LC}, P_{T} and P_{I} correspond to the left circularly polarized scattered power, the total scattered power and the incident power respectively, and $T = \frac{P_{\text{T}}}{P_{\text{I}}}$ is the transmittance.

The purity, ρ, is a measure of the extent to which the handedness of the scattered light is inverted with respect to the incident right circular polarization [45]. As such, it denotes how 'pure' the scattered light is in terms of the inverted polarization handedness. For instance, $\rho = 1$ when the handedness of scattered light is completely inverted to left circularly polarized light, and $\rho = 0$ when the handedness of the scattered light is not inverted at all. The purity depends on both the scattering cross-section and phase of each eigenmode, and is unity when the scattered powers are equal and the phase difference, $\Delta\Phi$, is π.

For each design, we ran separate simulations with the source polarized along each eigenmode axis of the antenna. The fields transmitted by the array were recorded 4.2 μm above the plane of the antenna array. We combined the field components with the appropriate phase shift to calculate the equivalent response to a right circularly polarized input. We then projected the polarization of the combined response on left circular polarization to calculate ρ and η. In the following, we discuss the impact of varying the design parameters on ρ and η.

2. Effect of varying the parameters

For the following discussion, the topology parameter θ is set to 45° unless noted otherwise. We divide the discussion of the effect of varying each parameter into two domains, depending

on the strength of inter-antenna coupling, which critically depends on the inter-antenna spacing. We define the weak inter-particle coupling domain, within which changing *a* does not significantly shift the resonance wavelength of each eigenmode, and the strong inter-particle coupling domain, where the resonance wavelengths do shift when changing *a*. We also assume that $\Delta\Phi$ is smaller than π and therefore aim to maximize $\Delta\Phi$. We study the behavior of the parameter space systematically by varying one parameter at a time.

2.1. Effect of changing the lattice constant (a)

In the weak inter-particle coupling domain, increasing *a* does not significantly shift the resonance wavelength of the eigenmodes as shown in figure 3. Hence the $\Delta\Phi$ and ρ profiles do not spectrally shift. Since the inter-antenna coupling weakens due to the increased inter-antenna spacing, the damping is reduced and the resonance linewidth narrows. Consequently, the phase shift imparted by each eigenmode is reduced in the overlap region, reducing $\Delta\Phi$ and hence ρ, as shown in figures 3(b) and (c). Moreover, the width of the $\Delta\Phi$ profile remains the same, since it depends on the spectral gap between the eigenmodes. Hence the width of the ρ profile does not change significantly either.

In the strong inter-particle coupling domain, however, increasing *a* not only reduces the damping, it also results in a blue-shift of the resonance frequencies towards those of the isolated antenna, due to the near-field coupling present in this regime [46], thereby blue-shifting $\Delta\Phi$ and ρ. We observe that the symmetric resonance blue-shifts more than the antisymmetric one. This is because the symmetric resonance has stronger fields on the corners of the antenna (figure 1(c)), and hence is more strongly coupled to the neighboring antennas. The discrepancy in the spectral shift of each resonance increases the spectral gap between them, and thus broadens and reduces both $\Delta\Phi$ and ρ, as shown in figures 3(e) and (f).
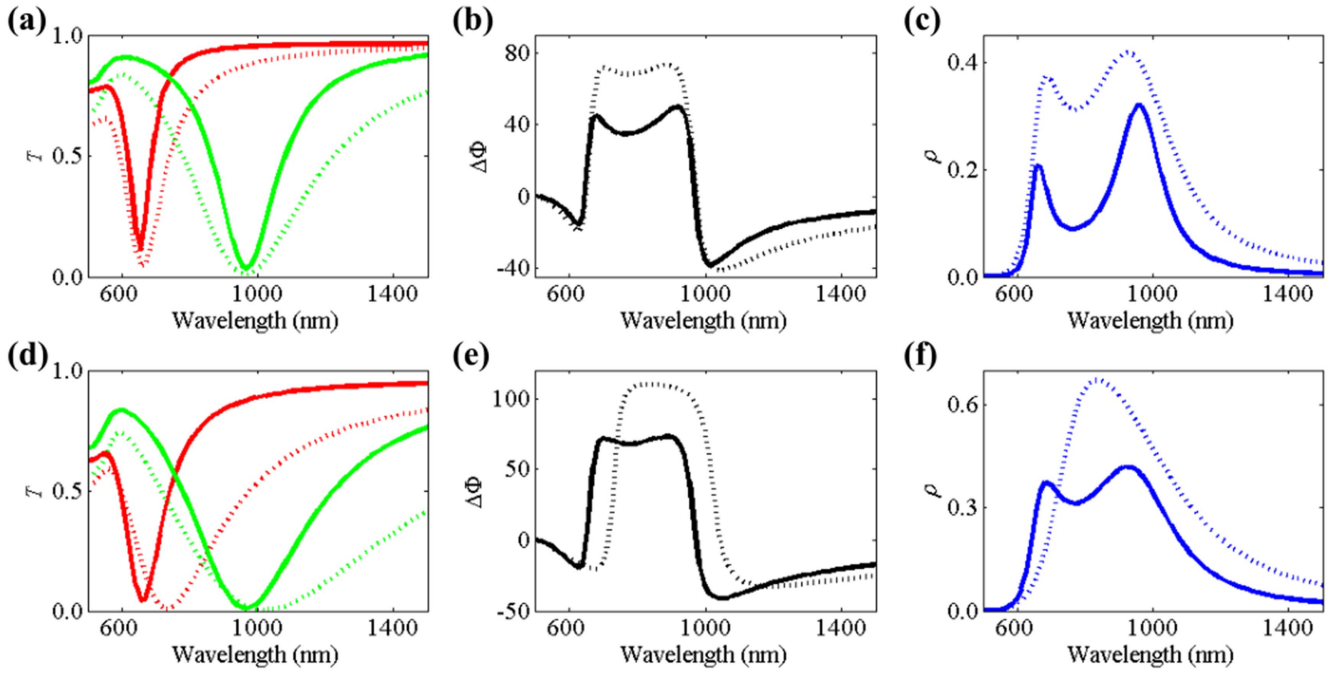
Figure 3. (a)–(c): Effect of increasing the period, *a*, in the weak inter-particle coupling domain. *T*, $\Delta\Phi$, and ρ are shown for $a = 200$ nm (dotted lines) and $a = 280$ nm (solid lines). Other antenna dimensions are $L = 140$ nm, $w = 40$ nm. Each resonance narrows but its central wavelength does not change. Consequently, the width of $\Delta\Phi$ and ρ does not change. Due to narrower resonances, $\Delta\Phi$ and hence ρ reduces. (d)–(f): Effect of increasing the period in the strong inter-particle coupling domain. *T*, $\Delta\Phi$ and ρ for $a = 160$ nm (dotted lines) and $a = 200$ nm (solid lines). Other antenna dimensions are $L = 140$ nm, $w = 40$ nm. Increasing the period blueshifts the symmetric eigenmode more than the antisymmetric one, thereby increasing the spectral spacing between the two resonance centers. The resonances also become narrower. Both of these effects reduce $\Delta\Phi$ and hence ρ.

Moreover, the resonances become narrower which also contributes to reducing $\Delta\Phi$ and ρ.

For very small inter-antenna gaps the resonances are very broad due to very strong inter-antenna coupling, and they narrow as the lattice constant is increased. For instance, figure 3(a) shows that increasing the lattice constant by 80 nm in the weak inter-particle coupling domain decreases the full-width-half-maximum (FWHM) roughly from 33 to 30 nm for the symmetric mode and from 44 to 39 nm for the antisymmetric mode, whereas in the strong inter-particle coupling domain increasing the lattice constant by just 40 nm decreases the FWHM roughly from 42 to 33 nm for the symmetric mode and from 93 to 44 nm for the antisymmetric mode. The broader resonances in the strong inter-particle coupling domain lead to an increased spectral overlap of the two eigenmodes, thereby providing a larger $\Delta\Phi$ and ρ. Consequently, the strong inter-particle coupling domain generally affords a larger ρ as compared to the weak inter-particle coupling domain.

2.2. Effect of increasing the antenna's arm length (*L*)

In either domain, increasing *L* gives rise to two contrary effects on $\Delta\Phi$ and ρ. Since the resonance wavelength scales with the arm length [33], increasing *L* red-shifts the resonances. Consequently, the spectra of $\Delta\Phi$ and ρ red-shift. Since the antisymmetric eigenmode spans across both arms of the antenna, whereas the symmetric eigenmode spans across only one, the antisymmetric resonance red-shifts more than the symmetric one (figure 4). Hence, the spectral spacing

between these resonances increases, which reduces and broadens $\Delta\Phi$ and ρ. However, a larger *L* reduces the inter-antenna spacing, which broadens the resonances and thus increases $\Delta\Phi$. These are competing effects and thus the net change in $\Delta\Phi$ and ρ depends on which effect dominates for a given set of antenna dimensions.

In the strong inter-particle coupling domain (figures 4(d)–(f)), we observe that each eigenmode red-shifts more than in the weak inter-particle coupling domain for the same increase in *L*. This is because in the strong inter-particle coupling domain the increase in *L* leads to stronger inter-antenna coupling that also contributes to the red-shift of the resonances. As explained earlier, the inter-antenna coupling shifts the symmetric resonance more than the antisymmetric one. Consequently, the increment in the spectral spacing between the resonances is less pronounced as compared to that in the weak inter-particle coupling domain. Hence, decrease in $\Delta\Phi$ and ρ due to an increase in the inter-resonance spectral spacing is less pronounced in the strong inter-particle coupling domain. On the other hand, the resonances broaden more, for the same reduction in inter-antenna spacing, due to the very strong near-field coupling (figure 4(c)). This gives a large positive contribution to $\Delta\Phi$ and ρ. Consequently, a larger $\Delta\Phi$ and ρ can be obtained in the strong inter-particle coupling domain.

2.3. Effect of increasing the antenna's arm width (*w*)

Increasing *w* for a fixed *L* makes the L-antenna more like a square, for which the spectra of the two orthogonal eigenmodes
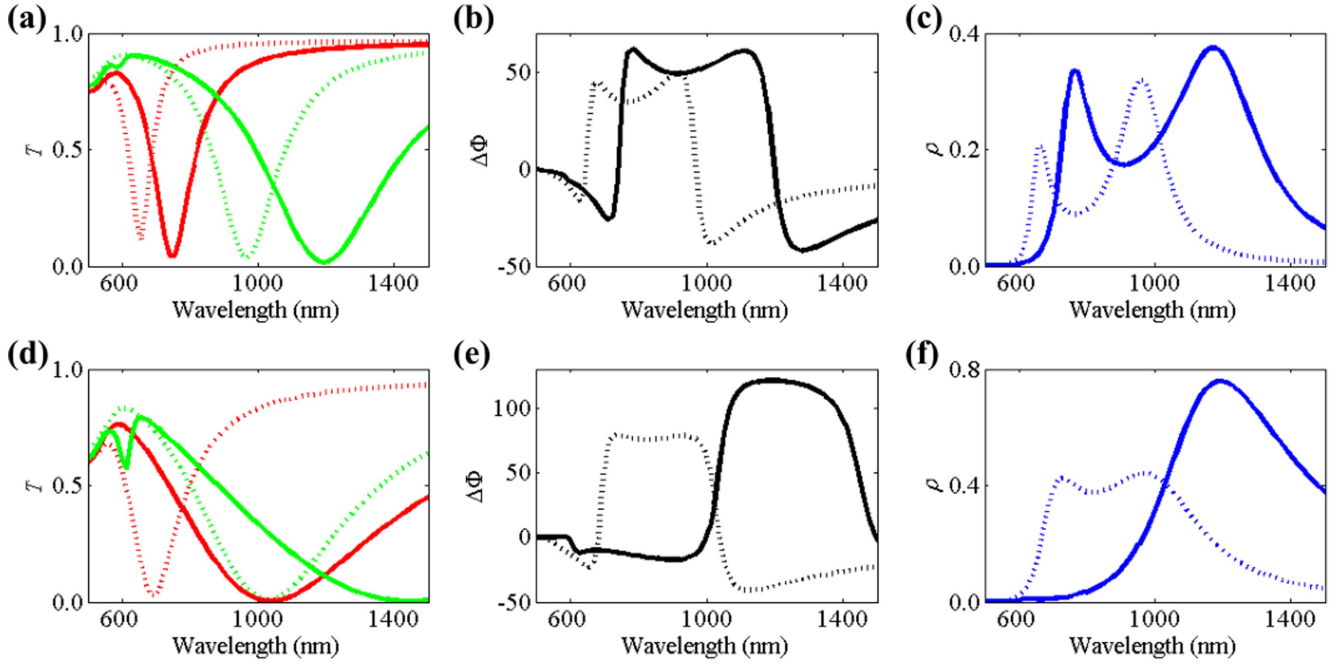
Figure 4. (a)–(c): Effect of increasing the arm length, L, in the weak inter-particle coupling domain. T, $\Delta\Phi$, and ρ for $L = 140$ nm (dotted lines) and $L = 180$ nm (solid lines). Other array dimensions are $w = 40$ nm and $a = 280$ nm. The symmetric resonance redshifts more than the antisymmetric one. This increases the spectral spacing between them, and thus broadens $\Delta\Phi$ and ρ. The resonances broaden and in this case the increase in $\Delta\Phi$, due to the broadening, dominates, resulting in an increased ρ. (d)–(f): Effect of increasing the arm length in the strong inter-particle coupling domain. T, $\Delta\Phi$ and ρ for $L = 150$ nm (dotted lines) and $L = 190$ nm (solid lines). Other array dimensions are $w = 40$ nm and $a = 200$ nm. Both eigenmodes red-shift more than in the weak inter-particle coupling domain for the same increase in length. Resonances are much broader. A high $\Delta\Phi$ and ρ are obtained.
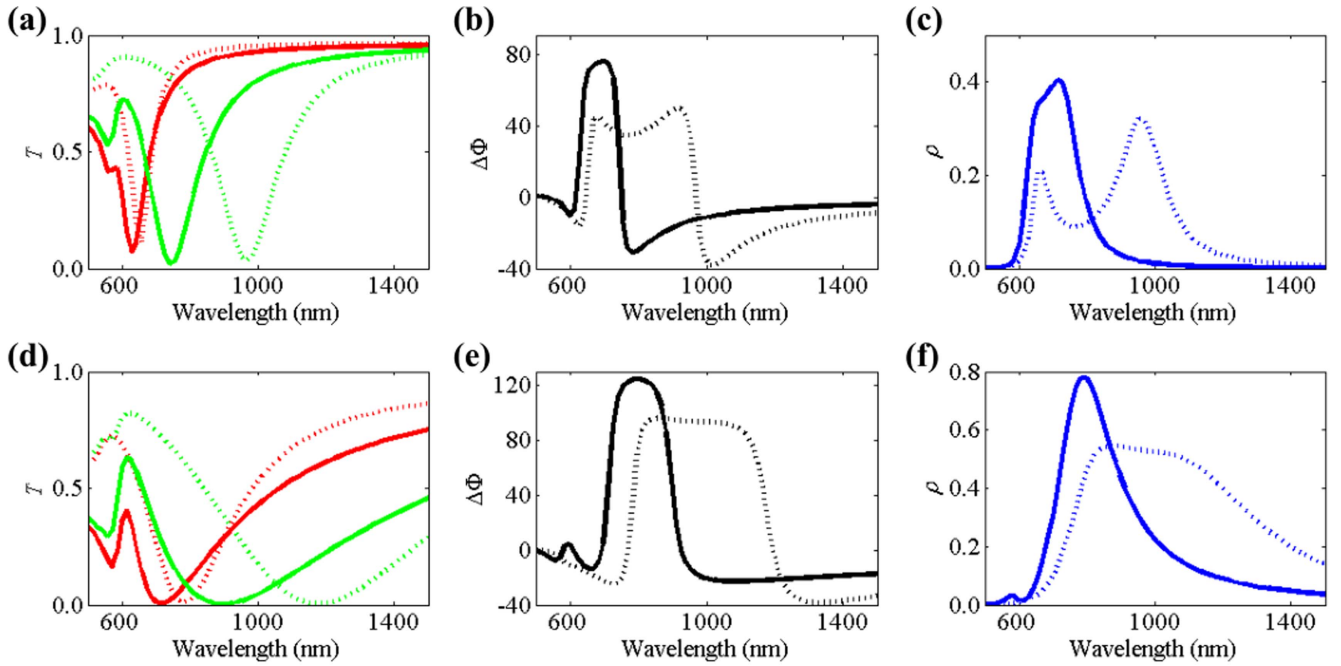

Figure 5. (a)–(c): Effect of increasing the arm width, w, in the weak inter-particle coupling domain. T, $\Delta\Phi$ and ρ for $w = 40$ nm (dotted lines) and $w = 80$ nm (solid lines). Other array dimensions are $L = 140$ nm and $a = 280$ nm. The symmetric resonance blue-shifts negligibly, whereas the antisymmetric resonance blue-shifts significantly. This reduces the spectral spacing between them and thus increases, and narrows, $\Delta\Phi$ and ρ. (d)–(f): effect of increasing the arm width in the strong inter-particle coupling domain. T, $\Delta\Phi$ and ρ for $w = 40$ nm (dotted lines) and $w = 80$ nm (solid lines). Other array dimensions are $L = 170$ nm and $a = 200$ nm. Both eigenmodes blue-shift and broaden more than in the weak inter-particle coupling domain, for the same increase in width. A high $\Delta\Phi$ and ρ are obtained.
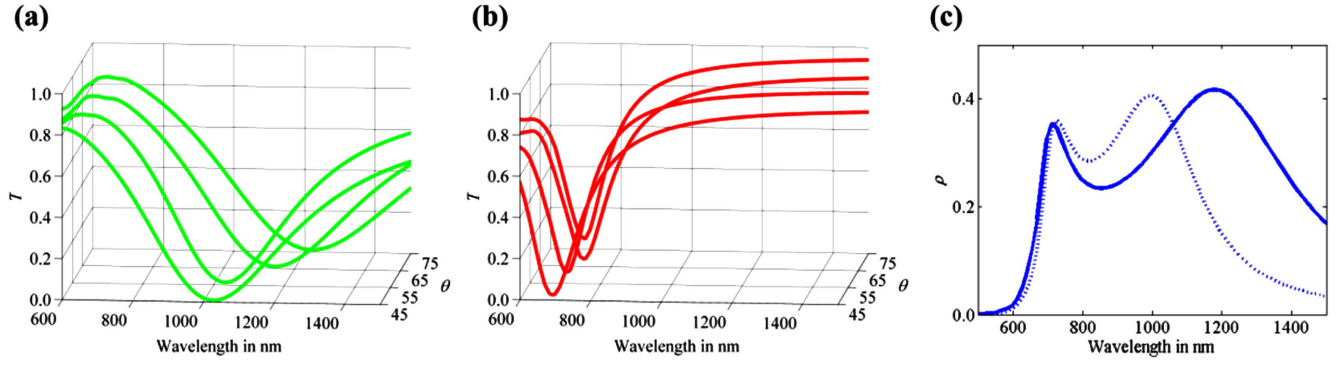
Figure 6. Effect of increasing the topology parameter θ in the strong inter-particle coupling domain on the transmittance of the (a) antisymmetric resonance and (b) the symmetric resonance. Increasing θ redshifts and broadens the antisymmetric resonance, while the overall effect on the symmetric resonance is small. (c): Effect of increasing θ from 55° (dotted curve) to 75° (solid curve) on the purity ρ. The antisymmetric resonance blueshifts and broadens (see figure 6(a)) whereas the symmetric resonance shows negligible change (see figure 6(b)). The resulting $\Delta\Phi$ and ρ broaden while roughly maintaining the same maximum value. Other array dimensions in (a)–(c) are $L = 150$ nm, $w = 40$ nm and $a = 200$ nm.

overlap perfectly. Therefore, in either coupling domain, increasing w decreases the spectral separation between the resonances as shown in figure 5. This reduced separation between the resonances narrows and increases $\Delta\Phi$ and ρ. Thus w can be used to trade-off between the bandwidth and ρ of the device. Moreover, the resonances blue-shift in either domain with increasing w. This is because the surface currents can deviate more from the arm axis and hence oscillate along shorter paths.

In the weak inter-particle coupling domain, the anti-symmetric resonance blue-shifts significantly whereas there is a negligible blue-shift in the symmetric resonance, as shown in figure 5(a). This shows that the antisymmetric resonance condition for 'fat' antennas is not accurately described by models based on a thin-wire approximation [36], which by its very nature cannot be used to model the effect of increasing w for a fixed L. In the strong inter-particle coupling domain, the stronger near field coupling results in a greater spectral shift and spectral broadening of both eigenmodes for the same increase in arm width, as shown in figure 5(d). A high $\Delta\Phi$ and ρ are obtained.

2.4. Effect of varying the array topology parameter (θ)

In the weak inter-particle coupling domain, the arrangement of the antennas relative to each other, and hence θ, only effects the linewidth of the eigenmodes. However, in the strong inter-particle coupling domain we observe that the antisymmetric resonance red-shifts and broadens as we increase θ from 45° (see figure 6(a)). This is because the ends of the neighboring antennas, which exhibit the strongest field localization for the antisymmetric mode (we refer back to figure 1(d)), move closer to one another. On the other hand, the symmetric resonance does not show a significant overall change as θ is varied (see figure 6(b)). The topology parameter can be tuned such that the antisymmetric resonance red-shifts and broadens due to stronger inter-antenna coupling while the symmetric resonance undergoes a negligible overall change, thereby providing a design parameter to increase the

bandwidth without significantly decreasing the maximum purity. In figure 6(c), we illustrate a specific example of this.

3. Results and discussion

Based on the effects of varying the design parameters as described above, we present a design methodology for moving the operating regime of a half-wave plate to a longer wavelength starting from any existing design. We focus on the weak inter-particle coupling domain, since it affords a larger inter-antenna spacing and hence more relaxed fabrication requirements.

To shift the eigenmodes, and hence ρ, to a longer wavelength, L has to be increased. However, this will reduce the inter-antenna spacing. Therefore, to increase L without departing from the weak inter-particle coupling domain, a should also be increased. This would maintain the width and spectral range of ρ but reduce its magnitude. Therefore a should not be made unnecessarily large. Next, L and w should be scaled up together to red-shift and increase ρ. Finally, w can be adjusted to trade-off the bandwidth with the maximum ρ. A larger w will narrow, increase and blue shift ρ. An example of the above recipe is presented in figure 7(a).

The above methodology also affords the possibility of designing an array having larger dimensions, and hence with more tolerance to fabrication constraints, but with the same η at a fixed design wavelength. While the center of the ρ and η profiles red-shift using the above methodology, their finite width can enable the final design to give the same η as the initial design at a fixed target wavelength. As an illustration, in figure 7(b) the final design has much larger antenna dimensions and inter-antenna spacing, but the same efficiency at 920 nm wavelength. We note that the peak efficiency of our design is comparable to the best reported half-wave plate efficiency for an ultrathin, single-layered planar plasmonic metasurface [16].

A similar design methodology can be used to design at a longer wavelength in the strong inter-particle coupling
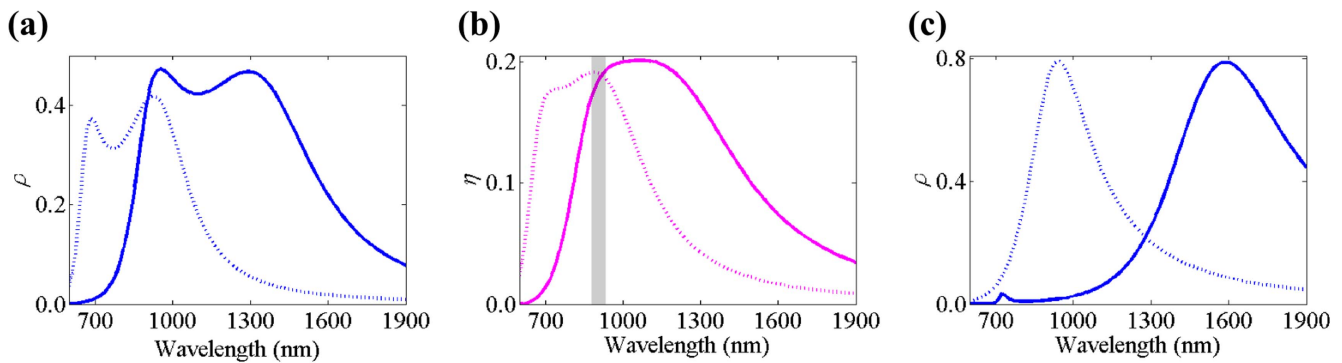
(a)   **(b)**   **(c)**

Figure 7. (a) Illustration of a recipe to design a half-wave plate at a longer wavelength in the weak inter-particle coupling domain. The design parameters are: $L = 140$ nm, $w = 40$ nm, $a = 200$ nm (dotted line) and $L = 270$ nm, $w = 80$ nm and $a = 360$ nm (solid lines). (b) Illustration of a recipe to design a half-wave plate to operate at the same wavelength (gray shading) with larger design parameters, for easier fabrication. The design parameters are: $L = 140$ nm, $w = 40$ nm, $a = 200$ nm (dotted line) and $L = 260$ nm, $w = 90$ nm and $a = 360$ nm (solid line). Both designs show the same efficiency at 920 nm wavelength. (c) Illustration of recipe to design at longer wavelength in strong inter-particle coupling domain. ρ is shown for $L = 140$ nm, $w = 40$ nm, $a = 150$ nm (dotted line) and $L = 290$ nm, $w = 60$ nm, $a = 300$ nm (solid line).

domain. This is viable when sophisticated fabrication processes are available. L needs to be increased to red-shift the eigenmodes and ρ. However, to increase L without touching the neighboring antenna, first a should be increased. This will blue-shift and reduce ρ. Increasing L will then red-shift and increase ρ. Finally, w and θ can be tailored to trade-off ρ with the bandwidth. As mentioned before, a higher ρ is obtained in this domain as compared to that in the weak inter-particle coupling domain. This recipe is illustrated in figure 7(c). We note that the recipes presented above are easily applicable to the design of quarter-wave plates as well.

We now discuss the practical utilty of our results in terms of current fabrication processes. The smallest antenna feature size we consider in this work is 40 nm, whereas the smallest inter-antenna gap we consider in our discussion of the weak inter-particle coupling domain is of 60 nm. These feature sizes can be easily realized through standard electron beam lithography (EBL). In the strong inter-particle coupling domain, the smallest inter-antenna gap we utilize is of 10 nm. This gap size can be reliably fabricated using focused ion beam lithography, but it is an expensive process and is thus applicable only to small area metasurfaces. However, gap sizes of 20 nm have been realized with EBL [47], and our discussion of the strong inter-particle coupling regime is valid at this gap size. Finally, we note that the difficulty of fabricating very small features signifies the methodology we present above, where we design arrays with larger dimensions but with the same efficiency at a desired wavelength.

4. Conclusion

In this work we have presented principles that can be used to design wave plate metasurfaces at a wavelength of choice and for diverse application requirements using arrays of L-shaped plasmonic antennas. We derive the design principles by studying the behavior of the vast parameter space of these antenna arrays, and demonstrate the importance of utilizing the array properties in the design process. We demonstrate the application of these principles through three examples: a wave plate design tailored to available fabrication capabilities and an adaptation of a design to a new operating frequency in each of the weak and strong inter-particle coupling regimes. In all cases we design for operation at a desired wavelength while having control over multiple device performance characteristics—the purity, the efficiency and the operating bandwidth. The results we present here are also applicable to designing quarter-wave plates, and can be extended to incorporate other parameters such as antenna thickness. This work will help readers develop insights into the properties of L-antenna arrays and enable a more effective design process for ultrathin wave plates.

References

[1] Marrucci L, Manzo C and Paparo D 2006 Optical spin-to-orbital angular momentum conversion in inhomogeneous anisotropic media *Phys. Rev. Lett.* **96** 163905
[2] Papakostas A, Potts A, Bagnali D M, Prosvirnin S L, Coles H J and Zheludev N I 2003 Optical manifestations of planar chirality *Phys. Rev. Lett.* **90** 107404
[3] Zhao Y, Belkin M A and Alù A 2012 Twisted optical metamaterials for planarized ultrathin broadband circular polarizers *Nat. Commun.* **3** 870
[4] Gansel J K, Thiel M, Rill M S, Decker M, Bade K, Saile V, von Freyman G, Linden S and Wegener M 2009 Gold helix photonic metamaterial as broadband circular polarizer *Science* **325** 1513–5
[5] Khlebtsov N G, Melnikov A G, Bogatyrev V A, Dykman L A, Alekseeva A V, Trachuk L A and Khlebtsov B N 2005 Can

the light scattering depolarization ratio of small particles be greater than 1/3? *J. Phys. Chem.* B **109** 13578–84

[6] Gopnzáles A L, Reyes-Esqueda J A and Noguez C 2008 Optical properties of elongate noble metal nanoparticles *J. Phys. Chem.* C **112** 7356−62

[7] Gryczynski Z, Lukomska J, Lakowicz J R, Matveeva E G and Gryczynski I 2006 Depolarized light scattering from silver nanoparticles *Chem. Phys. Lett.* **421** 189−92

[8] Calander N, Gryczynski I and Gryczynski Z 2007 Interference of surface plasmon resonances causes enhanced depolarized light scattering from metal nanoparticle *Chem. Phys. Lett.* **434** 326−30

[9] Shegai T, Li Z, Dadosh T, Zhang Z, Xu H and Haran G 2008 Managing light polarization via plasmon-molecule interactions within an asymmetric metal nanoparticle trimer *Proc. Natl Acad. Sci. USA* **105** 16448−53

[10] Hong-Ya C, Fu W-J, Hua M, Shao-Bo Q, Jie-Qui Z, Zhuo X and An-Xue Z 2015 Broadband perfect polarization conversion metasurfaces *Chin. Phys.* B **24** 014201

[11] Yu P, Chen S, Li J, Cheng H, Li Z, Liu W, Xie B, Liu Z and Tian J 2015 Generation of vector beams with arbitrary spatial variation of phase and linear polarization using plasmonic metasurfaces *Opt. Lett.* **40** 3229−32

[12] Iwami K, Ishii M, Kuramochi Y, Ida K and Umeda N 2012 Ultrasmall radial polarizer array based on patterned plasmonic nanoslits *Appl. Phys. Lett.* **101** 161119

[13] Chen X, Huang L, Mühlenbernd H, Li G, Bai B, Tan Q, Jin G, Qiu C-W, Zhang S and Zentgraf T 2012 Dual-polarity plasmonic metalens for visible light *Nat. Commun.* **3** 1198

[14] Young L, Robinson L and Hacking C A 1973 Meander-line polarizer *IEEE Trans. Antennas Propag.* **21** 376−8

[15] Strikwerda A C, Fanm K, Tao H, Pilon D V, Zhang X and Averitt R D 2009 Comparison of birefringent electric split-ring resonator and meanderline *Opt. Express* **17** 136−49

[16] Wadsworth S L, Clem P G, Branson E D and Boreman G D 2011 Broadband circularly-polarized infrared emission from multilayer metamaterials *Opt. Mater. Express* **1** 466−79

[17] Li T, Liu H, Wang S-M, Yin X-G, Wang F-M, Zhu S-N and Zhang X 2008 Manipulating optical rotation in extraordinary transmission by hybrid plasmonic excitations *Appl. Phys. Lett.* **93** 021110

[18] Pors A, Nielsen M G, Della Valle G, Willatzen M, Albrektsen O and Bozhevolnyi S I 2011 Plasmonic metamaterial wave retarders in reflection by orthogonally oriented detuned electrical dipoles *Opt. Lett.* **36** 1626−8

[19] Zhao Y and Alù A 2013 Tailoring the dispersion of plasmonic nanorods to realize broadband optical meta-waveplates *Nano Lett.* **13** 1086−91

[20] Shao J, Li J, Wang Y-H, Li J-Q, Chen Q and Dong Z-G 2014 Polarization conversions of linearly and circularly polarized lights through a plasmon-induced transparent metasurface *J. Appl. Phys.* **115** 243503

[21] Sieber P E and Werner D H 2014 Infrared broadband quarter-wave and half-wave plates synthesized from anisotropic Bézier metasurfaces *Opt. Express* **22** 32371

[22] Chen W, Tymochenko M, Gopalan P, Ye X, Wu Y, Zhang M, Murray C B, Alù A and Kagan C R 2015 Large-area nanoimprint colloidal Au nanocrystal-based nanoantennas for ultrathin polarizing plasmonic metasurfaces *Nano Lett.* **15** 5254−60

[23] Jiang Z H, Lin L, Ma D, Yub S, Werner D H, Liu Z and Mayer T S 2014 Broadband and wide field-of-view plasmonic metasurface-enabled waveplates *Sci. Rep.* **4** 7511

[24] Jiang S-C, Xiong X, Hu Y-S, Hu Y-H, Ma G-B, Peng R-W, Sun C and Wang M 2014 Controlling the polarization state of light with a dispersion-free metastructure *Phys. Rev.* X **4** 021026

[25] Ding F, Wang Z, He S, Shalaev V M and Kildishev A V 2015 Broadband high-efficiency half-wave plate: a supercell-based plasmonic metasurface approach *ACS Nano* **9** 4111−9

[26] Kim J, Choudhury S, DeVault C, Zhao Y, Kildishev A V, Shalaev V M, Alu A and Boltasseva A 2016 Controlling the polarization state of light with plasmonic metal oxide metasurface *ACS Nano* **10** 9326−33

[27] Shaltout A, Liu J, Shalaev V M and Kildishev A V 2014 Optically active metasurface with non-chiral plasmonic nanoantennas *Nano Lett.* **14** 4426−31

[28] Kildishev A V, Boltasseva A and Shalaev V M 2013 Planar photonics with metasurfaces *Science* **339** 1289

[29] Xu Q, Bao J, Rioux R M, Perez-Castillejos R, Capasso F and Whitesides G M 2007 Fabrication of large-area patterned nanostructures for optical applications by nanoskiving *Nano Lett.* **7** 2800−5

[30] Sung J, Sukharev M, Hicks E M, Van Duyne R P, Seideman T and Spears K G 2008 Nanoparticle spectroscopy: birefringence in two-dimensional arrays of L-shaped silver nanoparticles *J. Phys. Chem.* C **112** 3252−60

[31] Yu N, Aieta F, Genevet P, Kats M A, Gaburro Z and Capasso F 2012 A broadband, background-free quarter-wave plate based on plasmonic metasurfaces *Nano Lett.* **12** 6328−33

[32] Black L-J, Wang Y, de Groot C H, Arbouet A and Muskens O L 2014 Optimal polarization conversion in coupled dimer plasmonic nanoantennas for metasurfaces *ACS Nano* **8** 6390−9

[33] Yu N, Genevet P, Kats M A, Aieta F, Tetienne J-P, Capasso F and Gaburro Z 2011 Light propagation with phase discontinuities: generalized laws of reflection and refraction *Science* **334** 333−7

[34] Karimi E, Schulz S A, De Leon I, Qassim H, Upham J and Boyd R W 2014 Generating optical orbital angular momentum at visible wavelengths using a plasmonic metasurface *Light: Sci. Appl.* **3** e167

[35] Bouchard F, De Leon I, Schulz S A, Upham J, Karimi E and Boyd R W 2014 Optical spin-to-orpital angular momentum conversion in ultra-thin metasurfaces with arbitrary topological charges *Appl. Phys. Lett.* **105** 101905

[36] Blanchard R, Aoust G, Genevet P, Yu N, Kats M A, Gaburro Z and Capasso F 2012 Modeling nanoscale V-shaped antennas for the design of optical phased arrays *Phys. Rev.* B **85** 155457

[37] Gudjonson H, Kats M A, Liu K, Nie Z, Kumacheva E and Capasso F 2013 Accounting for inhomogeneous broadening in nano-optics by electromagnetic modeling based on Monte Carlo methods *Proc. Natl Acad. Sci. USA* **111** E639−44

[38] Bomzon Z, Biener G, Kleiner V and Hasman E 2002 Space-variant Pancharatnam–Berry phase optical elements with computer-generated subwavelength gratings *Opt. Lett.* **27** 1141−3

[39] Slussarenko S, Alberucci A, Jisha C P, Piccirillo B, Santamato E, Assanto G and Marucci L 2016 Guiding light via geometric phases *Nat. Photon.* **10** 571−5

[40] Lin D, Fan P, Hasman E and Brongersma M L 2014 Dielectric gradient metasurface optical elements *Science* **345** 298−302

[41] Yu N and Capasso F 2014 Flat optics with designer metasurfaces *Nat. Mater.* **13** 139–50

[42] https://lumerical.com/

[43] Johnson P B and Christy R W 1972 Optical constants of the noble metals *Phys. Rev.* B **6** 4370

[44] Palik E D 1997 *Handbook of Optical Constants of Solids* (New York: Academic)

[45] Schulz S A, Upham J, Bouchard F, De Leon I, Karimi E and Boyd R W 2015 Quantifying the impact of proximity error correction on plasmonic metasurfaces *Opt. Mater. Express* **5** 2798–803

[46] Romero I, Azipurua J, Bryant G W and de Abajo F J G 2006 Plasmons in nearly touching metallic nanoparticles: singular response in the limit of touching dimers *Opt. Express* **14** 9988

[47] Vieu C, Carcenac F, Pepin A, Chen Y, Mejias M, Lebib A, Manin-Ferlazzo L, Couraud L and Launois H 2000 Electron beam lithography: resolution limits and applications *Appl. Surf. Sci.* **164** 111–7